Correlation between quenching rate, mechanical properties and microstructure in thick sections of Al Mg Si(Cu) alloys

Victor Garric, Kimberly Colas, Patricia Donnadieu, Gilles Renou, Stéphane Urvoy, Bénédicte Kapusta

Correlation between quenching rate, mechanical properties and microstructure in thick sections of Al-Mg-Si(-Cu) alloys

Victor Garric[a], Patricia Donnadieu[c], Gilles Renou[c], Stéphane Urvoy[b], Kimberly Colas[a], Bénédicte Kapusta[a]

[a] *DEN-Service d'Etudes des Matériaux Irradiés, CEA Université Paris-Saclay, F-91191, Gif-sur-Yvette, France*
[b] *DEN-Service de Recherches Métallurgiques Appliquées, CEA Université Paris-Saclay, F-91191, Gif-sur-Yvette, France*
[c] *Univ. Grenoble Alpes, CNRS, Grenoble INP, SIMaP F-38000 Grenoble, France*

Abstract

Thermal treatment is key for the mechanical behavior of 6000 series aluminum alloys. Numerous studies have therefore been devoted to the impact of aging treatment parameters like time and temperature. However the influence of quenching rate is rather poorly documented while it could be of primary interest for applications requiring thick sections. Using a series of Al-Mg-Si(-Cu) specimens quenched in various fluids, we propose to monitor and describe the quench properly and study the impact of the quenching rate on the microstructure and mechanical properties obtained after aging. Acknowledging the critical quench rate to be about 10°C.s^{-1}, quenching was performed in various quenching fluids (water, air and oil) on 10cm side 6061 alloy cubes. The quench rate was evaluated by thermocouples placed at several locations and by numerical modeling. For each temper, the microstructure and mechanical behavior has been studied at local and macro scales to highlight some correlations. The combination of transmission electron microscopy imaging and related image analysis, chemical and crystallographic mapping, microhardness maps and tensile tests has pointed out many microstructural differences at nanoscale and inhomogeneous mechanical behavior we strived to explain and correlate.

Keywords: aluminum alloys, thermal treatment, microstructure, 6061

1. Introduction

With growing interest in Al-Mg-Si(-Cu) alloys in the automotive industry and the understanding of hardening precipitation (Jacobs et al. [1], Ryum et al. [2], Murayama et al. [3], C.Barbosa [4], Banhart et al. [5]) and the different effects of silicon/magnesium excess (Matsuda et al. [6], Ding et al. [7], Jaafar et al. [8]), many studies about control and improvement of thermal treatments and its link with mechanical properties have been made (Abúndez et al. [9], Farshidi et al. [10], Ma et al. [11], Ambriz et al. [12], Maisonnette et al. [13], Mrówka-Nowotnik and Sieniawski [14]). Among those, few focus on the influence of the quench (Cavazos and Colás [15, 16], Strobel et al. [17]) in addition, since most of these works have been conducted on thin samples the quenching rate variation across thickness is not a key parameter. The critical cooling rate (v_{crit}) of such alloys is known to be about 10°C.s^{-1} and it there a general consensus that a higher cooling rate would have no significant influence while a lower would lead to poorer mechanical properties (Davis and Committee [18], Totten and MacKenzie [19]). However, recent investigations (Schumacher et al. [20], Dutta and Allen [21]) using Differential Scanning Calorimetry (DSC) and earlier experiments (Ryum et al. [2]) tend to contests those assumptions and suggests v_{crit} would not be a plain boundary. They suggest the existence of two borders: a Lower Critical Cooling Rate (LCCR) under which every element in solution would precipitate and an Upper Critical Cooling Rate (UCCR), above which every element would be in a solid solution state. Thermal history are assumed to be not only influencing mechanical properties and hardening precipitates but also dispersoïd, known to have a very wide range of shape and phases (Buchanan et al. [22], Claves et al. [23], Wang et al. [24]). Considering the alloy itself, a 6061 aluminum alloy with copper addition was chosen in order to enhance the precipitation of hardening phases, to differentiate between quenches, but also to compare our results to the numerous ones existing on 6061-T6 alloy and its thermal treatments (Ding et al. [7], Saito et al. [25]).

To characterize these phenomenons, the following approach was chosen : first, three thick specimens where thermally treated and quenched in different fluids. The quench was monitored and modeled numerically in order to evaluate the quench rate at different position. Acknowledging the cooling rates, microstructural investigations were performed to understand the influence of the cooling rate on the microstructure whereas tensile tests and microhardness maps were carried out to evaluate its consequences on local and global mechanical properties.

Email addresses: victor.garric@cea.fr (Victor Garric), patricia.donnadieu@simap.grenoble-inp.fr (Patricia Donnadieu), gilles.renou@simap.grenoble-inp.fr (Gilles Renou), stephane.urvoy@cea.fr (Stéphane Urvoy), kimberly.colas@cea.fr (Kimberly Colas), benedicte.kapusta@cea.fr (Bénédicte Kapusta)

2. Material and methods

	Min	Optimum	Max
Mg	0.7	0.85	0.95
Si	0.4	0.48	0.56
Fe		0.05	0.12
Cu	0.24	0.30	0.36
Cr	0.25	0.30	0.35
Mn	0.02	0.08	0.14
Zn	530	0.05	0.10
$\sum$Ti, B, Li			<0.0675
Al		*balance*	

Table 1: Chemical composition of the studied alloy (%wt)

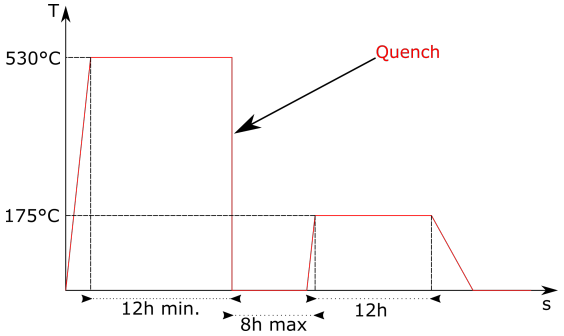

Figure 1: Thermal treatment for the three cubes

	x	y	z
I	49	34	**25**
II	49	49	**49**
III	49	64	**10**

Table 2: Probes positions (mm)

The 6061 alloy was received as a thick plate with the chemical composition specified in Table 1. The material was obtained by press forging and was thermally treated at 530°C for 4h then tempered at 175°C for 12h. Three cubes with a 98mm side have been cut in the as received thick plate, three thermocouples were placed in several positions of the cube as indicated in Table 2 with exception of the oil quench sample due to technical constraints. A thermal treatment which consists of a 12h annealing at 530°C followed by a quench in a different fluid for each cube (air, oil, water) and an artificial aging of 12h at 175°C (T6 temper) (Figure 1) with a maximum of 8 hours between the end of quench and the beginning of the artificial aging. During all the treatments, it has been considered that the treatment step begins were when the central probe reached the required temperature. To understand the quench and its future effects on the material, a numerical simulation with CAST3M (finite element software developped by CEACEA [26]) coupled with a Python routine was also used to evaluate the quench rate at every point on the cube.

To study the impact of quenching on the mechanical properties, a series of 50 tensile specimens was collected on each cube. Samples were 12x12x0.5 mm plates from the top center of a face to the center of a cube. TEM specimens were obtained by mechanical polishing to 100 microns using 1200 and 2400 grid paper , punching 3 mm discs and then eletropolishing using a 30% nitric acid solution at -20°C with a tension of 17V on a Tenupol-3. Tensile tests were performed with Instron 8862 with a deformation rate of $5.10^{-4}s^{-1}$. Vickers microhardness maps were performed using a Buehler VH-3300 automated microhardness indentation machine using 0.05 kg loading and 200 μm step on mirror polished samples representing the whole quench gradient for oil and water temper. TEM was performed using a FEI TECNAI-G2- 300kV LaB_6 and a JEOL-2100F - 200kV FEG for ASTAR (Rauch et al. [27, 28]) and EDS experiments.

3. Results

3.1. Quenching, measurements and numerical simulations

According to the cooling curves shown Figure 2a, for the air quench, the cooling rate appears to be homogeneous in the whole cube . The oil quench was performed in a sealed oven, which prevented recording of data. For water quench, the three cooling curves are given in Figure 2b. Experimental cooling rates have been calculated using a simple linear fitting function between 400°C and 200°C : $T = -v_q.t+a$, with v_q the quench rate. According to Figure 2a, with air quenching, the cooling curves are the same regardless of the position and the cooling rate in the 200-400°C range is $5.2°C.min^{-1}$. Water quench gives a range of quench rate from $39.6°C.s^{-1}$ to $22.6°C.s^{-1}$ (Table 3) : the quench rate in the center of the cube is given for information but wasn't taken in consideration in this study as many unexplained variations are seen in the experimental curve.

Depth	Water	Air
10mm	39.6	
25mm	29.6	$8.6.10^{-2}$
49mm	22.6	

Table 3: Quench rates ($°C.s^{-1}$)

Simulation of cooling curves of the water quench was performed using CAST3M using a fully meshed cube (98x98x98 mm) with cubic elements of 1.96x1.96x1.96 mm which gives a discretization of 125 000 elements. The following constants were fixed for the materials : thermal conductivity, λ= 167 $W.m^{-1}.K^{-1}$, heat capacity, c_p= 896 $J.kg^{-1}.K^{-1}$ and density ρ= 2700 $kg.m^{-3}$(Totten and MacKenzie [19]). While these values can easily be set as non time and temperature dependent, the heat transfer coefficient is extremely variable, and its determination not largely documented nor easily accessible (Cho

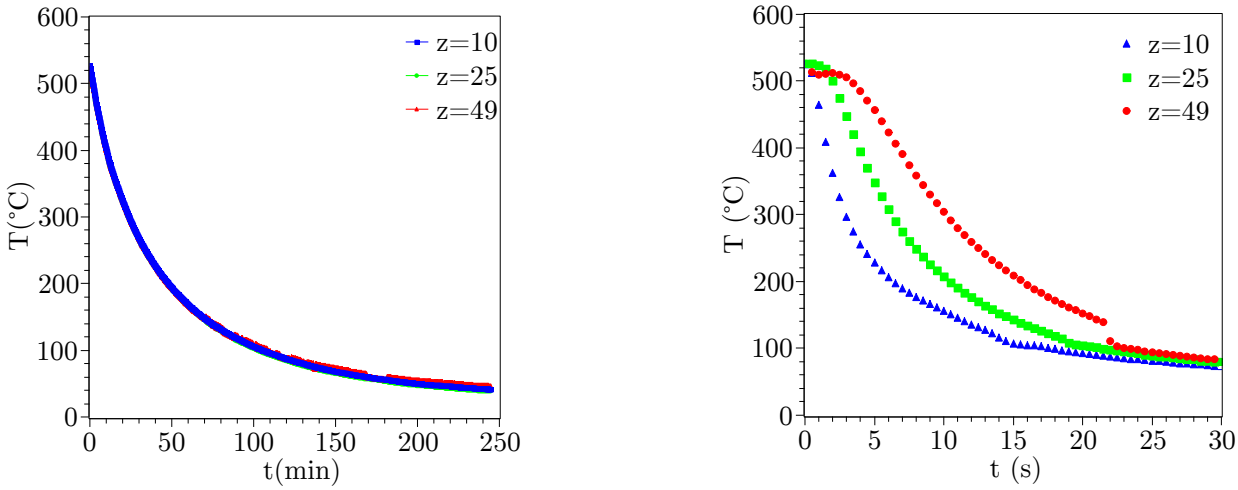

(a) Air sample

(b) Water sample

Figure 2: Quench : temperature vs time as recorded by thermocouples

[29]) :

$$h(t) = \frac{\rho V C_p}{A(T_s - T_\infty)} \frac{\partial T}{\partial t}(t)$$

With V the cube's volume, A its area, $T_s$the temperature before quenching and T_∞ the hypothetical temperature at the thermodynamic equilibrium. The heat capacity coefficient is given at the cube's surface. As the cooling curves where monitored inside the cubes, we propose a method to evaluate the heat transfer coefficient. Ignoring the temperature variation at the surface, a virtual coefficient, $h_{v,x}(t)$ is determined inside the cube. Knowing the shape of $h(t)$ to be similar as $h_{v,x\to 0}(t)$ an approximation of $h(t)$ can be determined in two steps :

1. Exponential regression on the maximum of the experimentally calculated $h_{v,x}(t)$, giving :

$$\begin{aligned} & max(h_v(t))(x) && \sim 1.8.10^4 e^{-z/10} + 3.10^3 \\ \Rightarrow \quad & max(h_v(t))(0) && \sim 21000 W.m^{-2}.K^{-1} \end{aligned}$$

2. Estimation for the $h(t)$ function, assuming the shape will be the same as the closest estimated $h_{v,x}(t)$ which is $h_{v,x=10}(t)$. We determined $\frac{max(h_v(t))(0)}{max(h_v(t))(0)} = 2.2$, giving the $h(t)$ function shown Figure 3.

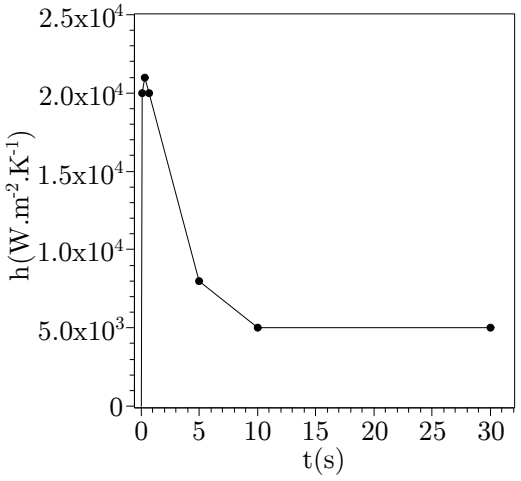

Figure 3: $h(t)$ calculated results for water quench

Figure 4a shows the superposed experimental and simulated T=f(t) curves at the same positions. The thermocouples at 10mm and 25mm depth (Table 3) are close to the model model while the difference between the curve at z=49 is assumed to be linked to an experimental issue. Acknowledging these results, a Python 3 script was coded in order to extract the data from CAST3M and calculate the cooling rate at every point. The curve shown in Figure 4b, pointed out a skin effect in the cube : the outer part shows a very fast drop of cooling rate whereas in the core part, no significant drop is seen. In addition, in every point of the water quench, the cooling rate is superior to the critical cooling rate ($10°C.s^{-1}$) while it is significantly lower in the air quench. Concerning the oil quench, as no suiTable data was obtained, the cooling rate is assumed to be lower than water quench and upper than air quench. This assumption will be developed during the microstructural investigations.

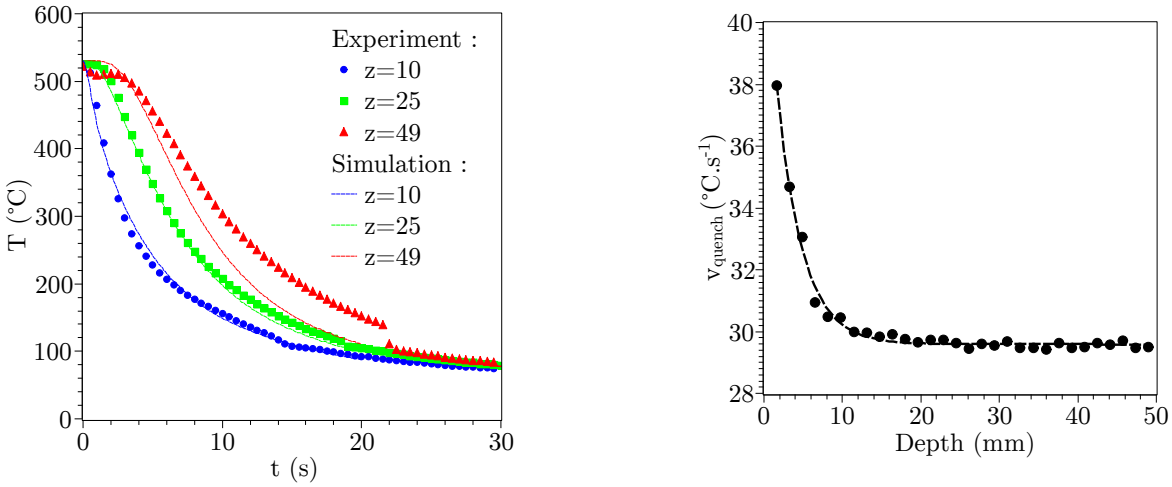

(a) Experimental vs simulated

(b) Cooling rate

Figure 4: Results of water quench simulations

3.2. Mechanical investigations

Tensile tests were carried out with a deformation rate of $5.10^{-4}s^{-1}$. The stress-strain on Figure 7, show two distinct behavior. The water and oil quench are close to the the behavior of a typical T6 temper with very slight differences. In the mean time, air quench exhibits significantly lower mechanical properties. Table 5 shows the elongation is the same in the three different quench. While the tensile tests specimens where obtained at different positions, no significant influence of this parameter was detected on the tensile properties.

Quench	Depth section	Mean	Standard deviation	Min.	Max	Indents
Water	Surface to 24.5mm	108	5	71	127	3630
	24.5mm to center	107	5	67	124	3596
Oil	Surface to 24.5mm	107	5	66	123	3491
	24.5mm to center	107	5	69	122	3841

Table 4: Summary of HV 0.05 maps for different regions in water and oil quench

In order to measure the microhardness, indentation maps have been carried out using a step of 200 μm. Data from the HV maps presented Table 4 pictures the expected value for the T6 temper and presented no significant influence of the thermal treatment at first glance. Nevertheless, a more local statistic study was conducted, plotting the hardness of three 5 mm wide areas : at the surface, first quarter and first half. In the distribution of the oil temper shown Figure 5a, no significant difference is pictured as the three distributions are overlying. Considering water temper, Figure 5b, the external distribution is shifted from the other ones. In a second time, hardness maps more or less the standard deviation were plotted (Figure 6). In this representation, oil temper (Figure 6b) presents a globally homogeneous map with extremely low hardness points, unexplained at first glance. The water temper seen in the distribution presents a wide range from the very to of the picture (49000 μm) to about 40000μm where the medium hardness is significantly higher than the rest of the specimen, confirming the results seen in the distribution.

Tensile tests tend to suggest oil and water temper tempers are globally equivalent in terms of mechanical properties. However, microhardness showed water temper presents locally higher hardness points while oil temper is more homogeneous : these results are emphasized and supported by microstructural investigations using TEM.

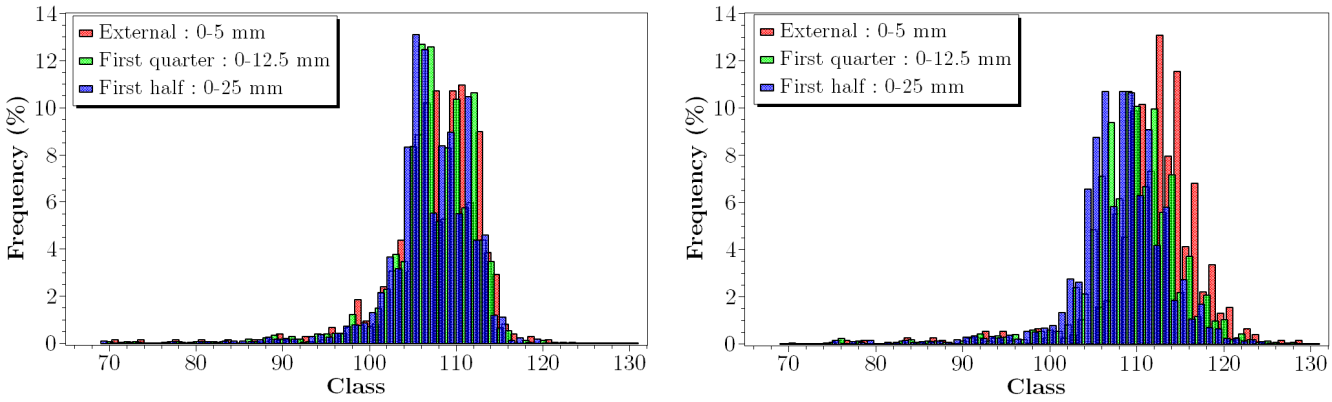

(a) Oil temper (b) Water temper

Figure 5: Microhardness distributions for each area

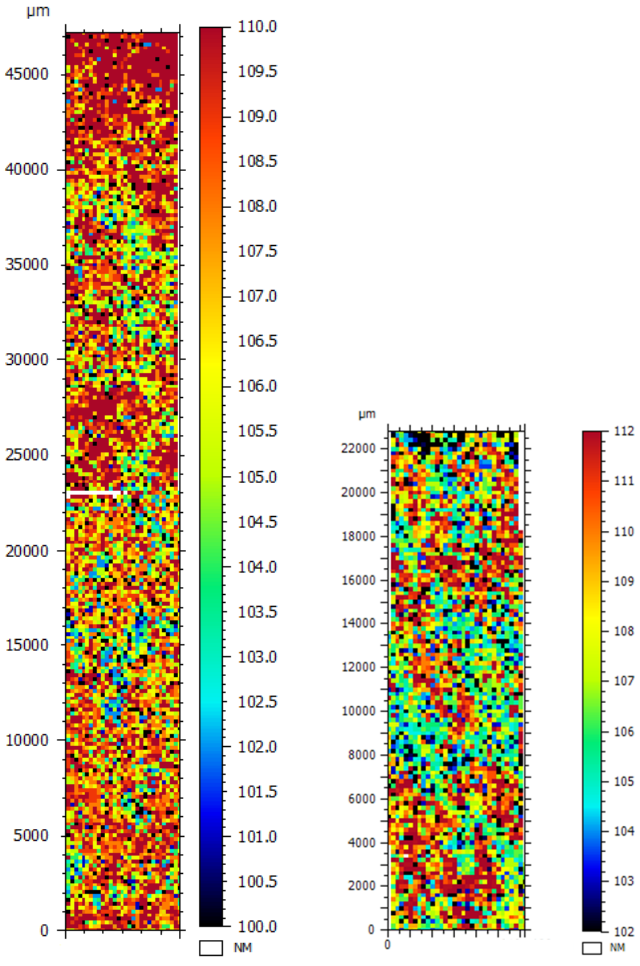

(a) Water temper (b) Oil temper

Figure 6: HV 0.05 maps

	Water	Oil	Air
$R_{p,0.2}$ (MPa)	232	230	100
R_m (MPa)	288	275	145
A (%)	13.5	12	11.75

Table 5: Mechanical properties in traction

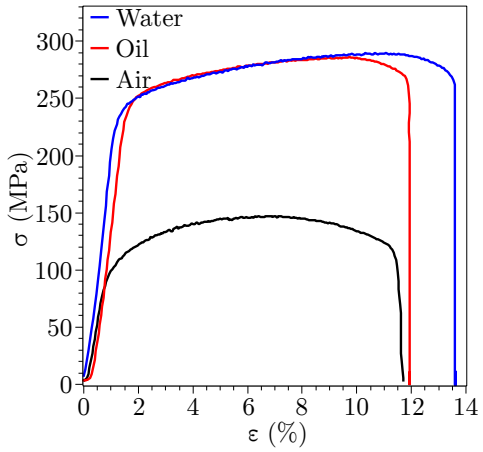

Figure 7: Medium traction behavior for the 3 quenches

3.3. Microstructural investigations

3.3.1. Water temper

Figure 8 highlights many aspects on the water quenched specimens at different positions and magnifications. First, Figure 8a presents the nanoscaled precipitation seen in the <100> zone axis. This precipitation presents many different populations : thin and elongated segments from 20 nm to 40 nm long with a medium thickness of 2.5 nm, round particles with a diameter of about 2.5 nm than can locally go up to 4.5 nm. Larger segments of about 3 nm but shorter, 6 nm to 10 nm, can be observed too. Thin segments are believed to be needles in 3D and small round particles to be the same particles seen in another direction. In other hand, smaller and larger segments are assumed to be rods in 3D and be linked with larger round particles seen another direction. Concerning the diffractogram, a long exposure pictures the peculiar signature of hardening precipitates (Mg_5Si_6) from 6xxx series. In other hand, an important contrast fluctuation is seen here, pointing out an heterogeneity, suggesting a local curvature in the sample. This could mean there is an important strain field around the precipitates. Concerning the influence of the depth at which the the sample was chose, *i.e* the influence of the quenching rate, Figure 8c and 8d show the hardening precipitates in dark field in a near surface sample (approximately 37°C.s^{-1} for quenching rate) and in a high depth sample (with 30°C.s^{-1} as quenching rate). It is clearly observable that a higher quenching rate gives a higher density of hardening precipitates. As illustrated by Figure 8b, the density of intermetallic particles significantly vary over a range of several microns. Also the mean radius of these particles is quite variable : from 30 nm to 300 nm on Figure 8b.This tendency seems to follow an opposite law of what can be observed for the nanoparticles : a higher cooling rate (near surface specimens) implies more and larger areas with a lack of intermetallics while a slower cooling rate (high depth specimens) pictures an uniform population of such particles. The chemical and crystallographic nature of the intermetallics seen in the water quench are α-AlMnFeCrSi plates and smaller phases already fully described in the literature (Lodgaard and Ryum [30]).

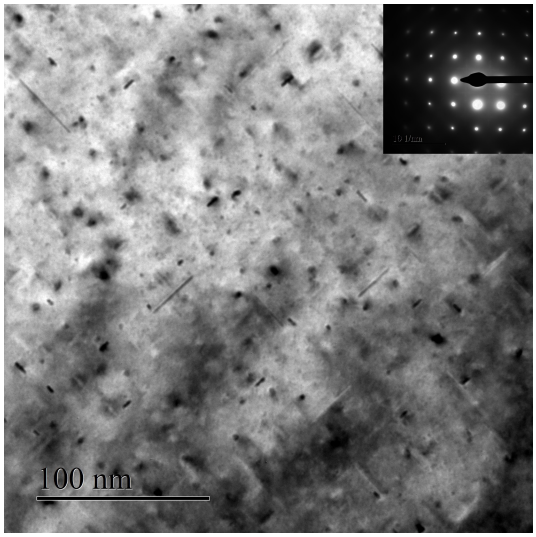

(a) Water temper : Nanoscaled precipitates

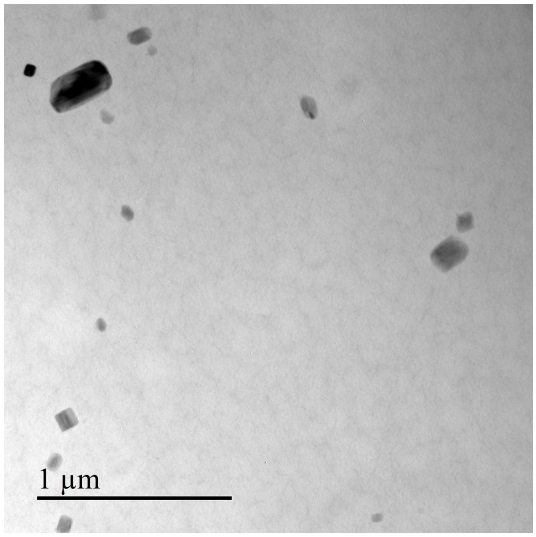

(b) Water temper : Microstructure at larger scale

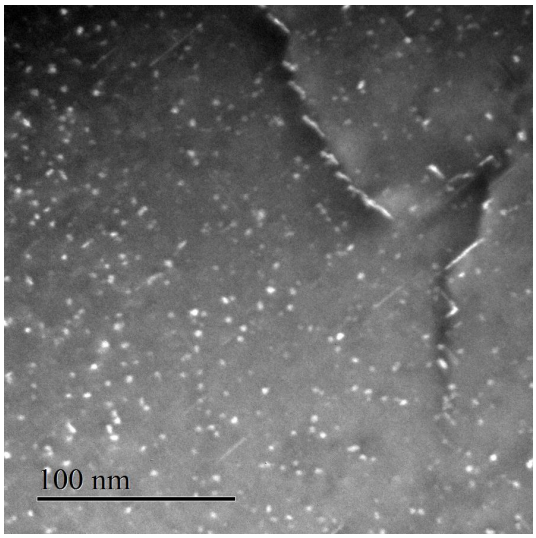

(c) Dark field on 001 Al reflexion in a near surface sample

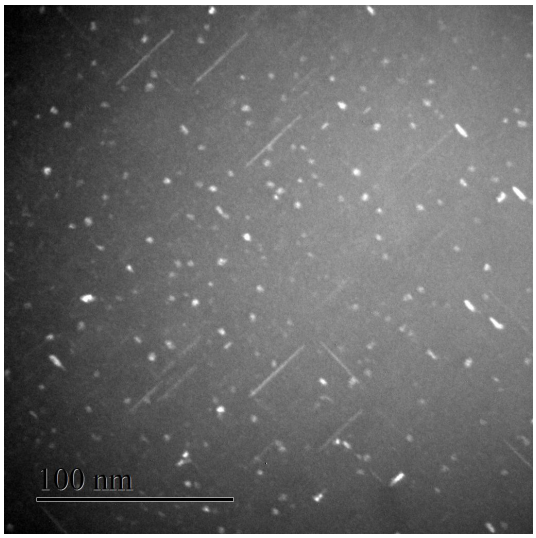

(d) Dark field on 001 Al reflexion in a half plate thickness sample

Figure 8: TEM pictures on water temper

3.3.2. Oil temper

Figure 9 presents the microstructure of oil temper at two different magnifications. Figure 9a presents nanoscaled precipitation similar to these observed in Figure 8a for water temper. The same families of nanoscaled precipitates are observed in terms of shapes, yet, the densities, length and thickness of the precipitates look different while the associated diffractogram pictures the same signature as seen in water temper. Elongated needles present the same length in a range of 20 nm to 40 nm, but their thickness doesn't seem to exceed 1 nm. In the mean time, rod like particles does not picture an higher length than 6 nm. In the case of oil temper the diffraction contrast look lighter around the precipitates picturing a softer strain field. Figure 9b presents the material seen at a lower magnification. The visual aspect of oil temper presents the same phases as in water temper with new elongated plates and new smaller phases not fully defined with a very heterogeneous background. These elongated plates do not exceed 250 nm in length and 30 nm width. Concerning the α phases seen in water temper, a difference is observed for the ones in the oil temper : very large dispersoïds of about 300 nm long are no longer observed and their size does go up to 180 nm maximum. Observing the precipitation and contrast, it can be assessed that a heterogeneous precipitation occured with different particles with various chemistry and crystallography growing on top of each other. Indeed, as it can be seen on Figure 10 which pictures the chemical heterogeneity of these particles is evidenced : it can be seen that silicon is present in all the dispersoïds while different

parts are highlighted with other elements. Magnesium is mostly present in the right part of the particle while the left side present oxygen as a major element.

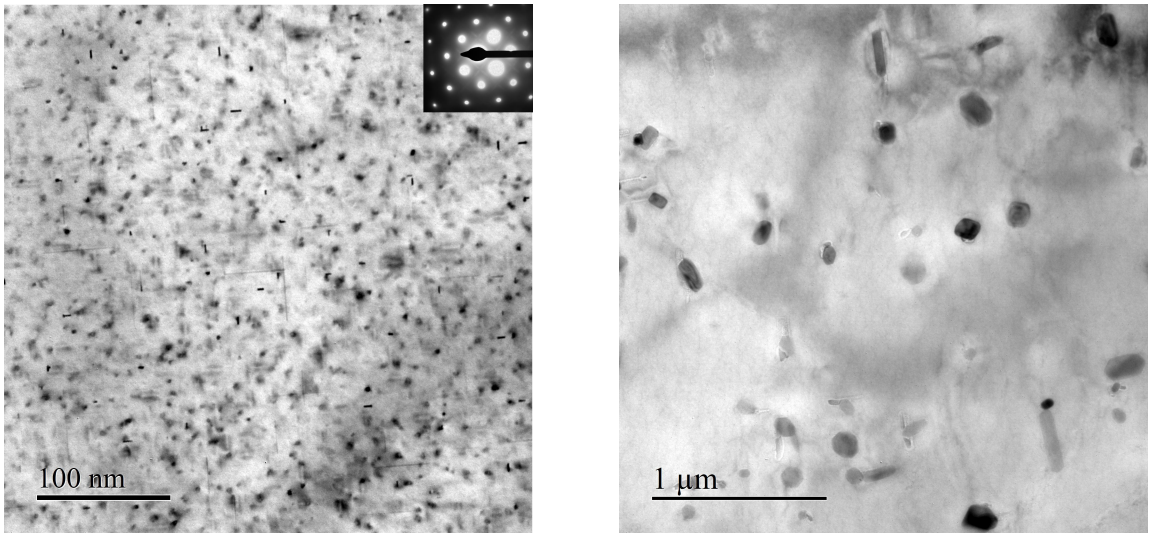

(a) Oil temper : Nanoscaled precipitates

(b) Oil temper : Microstructure at larger scale

Figure 9: TEM pictures on oil temper

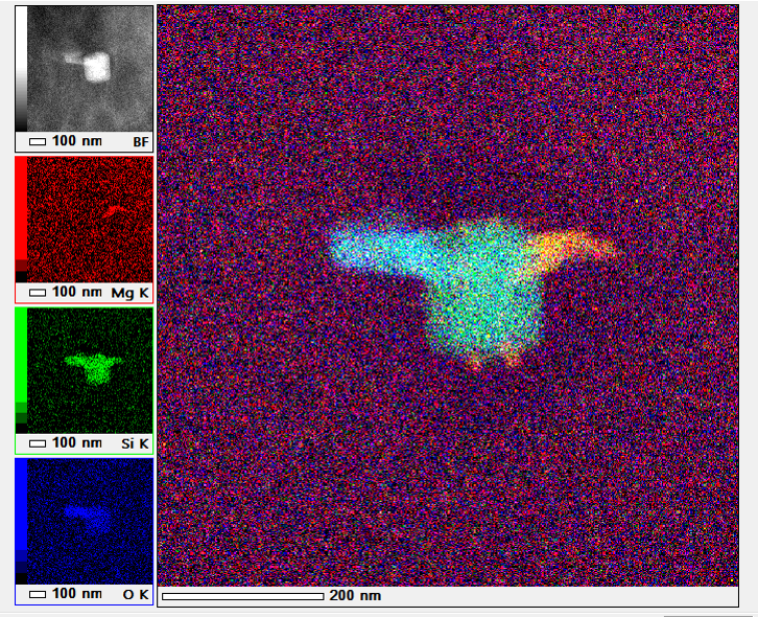

Figure 10: EDX on phases seen in oil temper

3.3.3. Air temper

Figure 11 pictures the microstructure of air temper at different scales. Figure 11a presents a dark field image on usual hardening phases spots in the <100> zone axis. As can be seen in Figure 11a, none of the usual nanoscaled phases are seen. However, very bright dots are seen on grain boundaries and dotted-line dislocations like presented here. Further

investigations with EDX analysis (Figure 13a) revealed an important enrichment of silicon and magnesium in these areas, suggesting a potential nano-precipitation on these very specific zones. Figure 11b pictures the microstructure at lower magnification : an extremely dense precipitation of intermetallics is observed with shapes and population not observed in the previous quenches. The population observed here can be divided in three populations : round and squareα-plates (already seen in water and oil tempers), heterogeneous particles of all size and shapes previously seen in oil temper and particularly long needle shaped plates are newly observed in air temper. These plates are up to 1000 nm long while their width goes from 50 nm for the longest to 200 nm for the least longs. EDS investigations on the heterogeneous particles (Figure 12), pictures no significant amount of magnesium while silicon is present in every type of phases. Like in oil temper, an important chemical heterogeneity and a composite formation of the dispersoïds is observed. Advanced characterization (ASTAR map which consist of a fine nanoprobe index of diffraction patterns along the a selected area coupled with crystallographic indexation in order to confirm phase identification using crystal databases defined by the userRauch et al. [28, 27], Figure 14) on needle shaped plates revealed a good accordance with precipitates of oxide of aluminum and magnesium. The ASTAR indexation failed in some parts of the needle. The diffraction patterns of the different areas indicates the precipitation of an unindexed phase in the needle but investigation on possible other crystal structures gave no significant results.

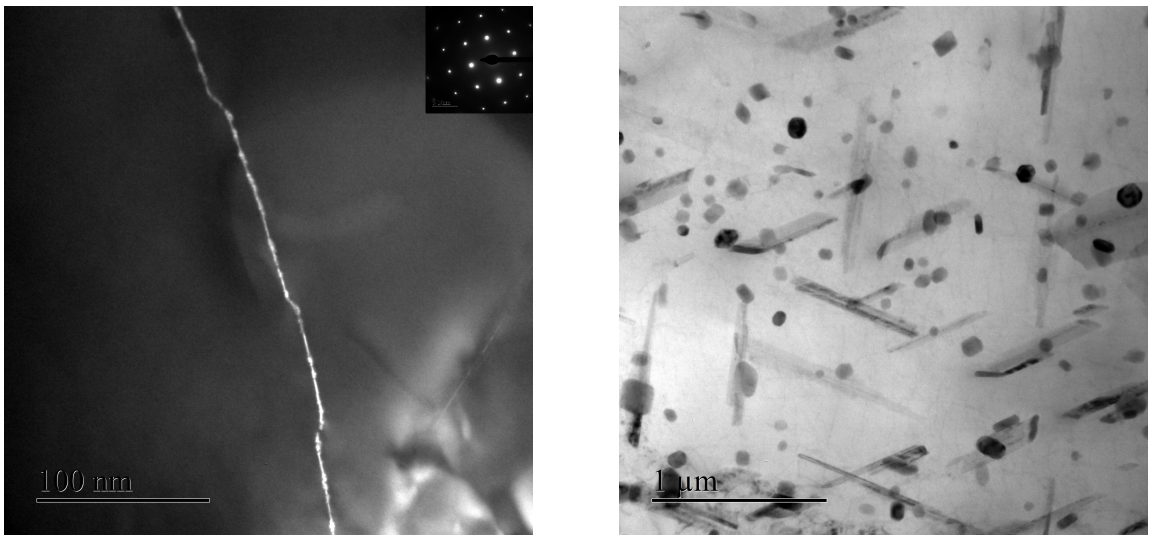

(a) Air temper : Nanoscaled precipitates seen along a dislocation seen in dark field

(b) Air temper : Microstructure at larger scale

Figure 11: TEM pictures on air temper

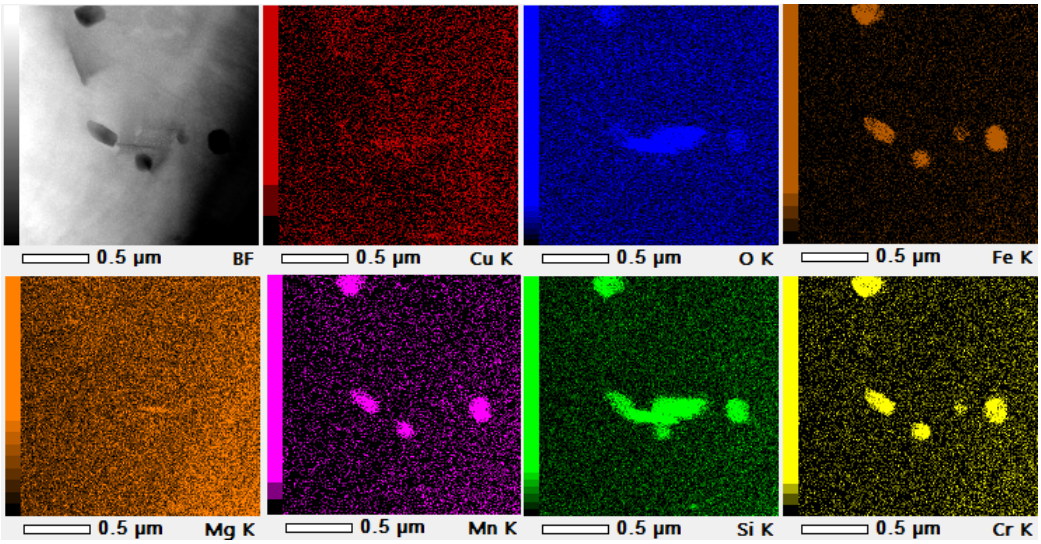

Figure 12: EDX on phases seen in air temper

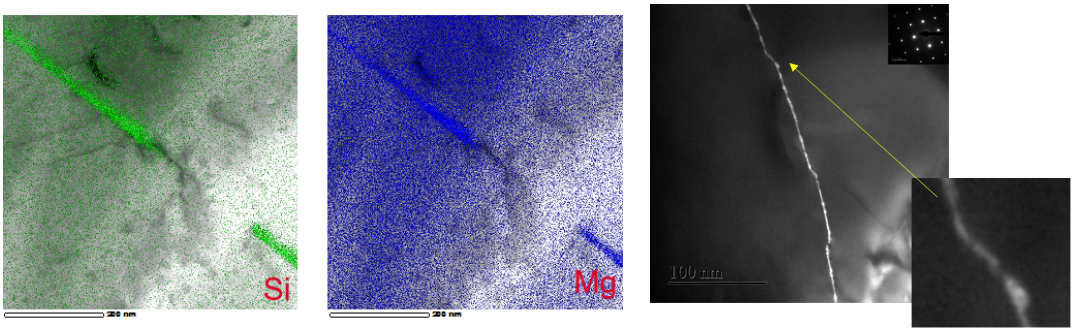

(a) EDX analysis along a dislocation

(b) Zoom on a dislocation along the direction {100}

Figure 13: EDX on dislocations in Air temper

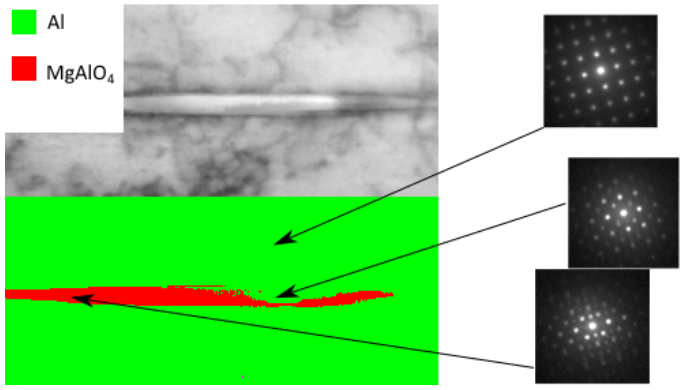

Figure 14: ASTAR analysis on a phase containing oxygen (air temper)

4. Discussion

Concerning the macro scale properties of thick sections of 6xxx aluminum alloys and its microstructure, the control of quenching rate is key. The state of art is giving leads of what are the consequences of badly controlled quenching in thin specimens. However, the heterogeneity, the microstructural mechanism and particularities leading to an inhomogeneous material remain unclear. Understanding the critical steps and effect happening in thick specimens is of primary interest for applications requesting thick sections. Also, pointing out the limit of the usual cooling rate, $10°C.s^{-1}$, for such applications is key.

In this study, the quench sensitivity of an Al-Mg-Si(-Cu) alloy was evaluated in a two step approach. First, a thermo-mechanical process with various quench fluids coupled with numerical simulation was carried out in order to reproduce and understand an industrial procedure. Finally, a microstructural and mechanical investigations (TEM, tensile tests, microhardness, EDS, ...) were done in order to understand the effects of the quench. Some important microstructural changes for each specimen and within each specimen has been highlighted. According to the literature, microstructural and mechanical changes are minor above $10°C.s^{-1}$. However, in the water temper sample, presenting a gradient of quenching rate above $10°C.s^{-1}$, microstructural differences were observed in the density of nanoscaled precipitation (Figure 8c and 8d). The microhardness maps (Figure 6) presented minor, yet, existent variation in the material behavior while the mechanical response in tensile test remain constant between the oil and water temper (Figure 5). Concerning the microstructural changes, oil temper and water temper presented differences in dispersoïds while both used to be over $10°C.s^{-1}$ in terms of quenching rate. EDS analysis on oil temper (Figure 10) presented an heterogeneous and composite precipitation around α plates while water temper presented clear and homogeneous α dispersoïds. Under $10°C.s^{-1}$, in air temper, the heterogeneity and the composite behavior is emphasized with growing density of dispersoïds (Figure 11b and 12). It has also been observed that, silicon was always present in such particles. Also, silicon is known to have a low solubility aluminum. Therefore we propose silicon to be the conditioning element of all the precipitation : a slow cooling rate will induce the presence of more silicon cluster, inducing a more coarse and heterogeneous precipitation of

dispersoïds around clusters, leading to fewer silicon available during the artificial aging and lower the density of nanoscaled precipitates. On the other hands, a higher cooling rate will induce a smaller density of dispersoïds and will allow the precipitation of more nanoscaled precipitates during the artificial aging. Even considering such a "soft area" to be non critical in a thick plate, the behavior of such plates under corrosive conditions is worrisome. As the green energy industry has considered 6xxx aluminum alloys as candidates for off-shore wind turbine materials, the potential presence of large dispersoïds is leading misbehavior of the material. As seen in Figure 14, high presence of oxygen was detected inside such particles. Its origin can be discriminated in two forms : First, we can consider the analysis to be relevant which induce the low cooling has leaded to the formation of oxides inside the material. As the presence of such phases was detected to be homogeneous in the whole material and oxygen was in an extremely low concentration prior to the thermomechanical treatment, this theory seemed to be poorly likely to occur. The second and most probable explanation is the fact that such large magnesium and silicon plates are extremely poorly resilient to corrosive environments and the oxides were formed during the specimens electropolishing. Consequently, a low quench rate surface exposed to a corrosive environment would lead to a highly destructive process for the material.

While these preliminary results are promising, more has to be carried out on the impact of such and heterogeneous precipitation behavior. If tensile tests results remain equivalent for both water and oil temper, more has to be done on other mechanical properties like fracture toughness. Moreover, the precipitation of dense dispersoïds like in air temper could have a very high impact on corrosion resistance. The presence of such "soft areas" inside thick sections of aluminum asses a potential danger for pieces made of such material, not only for the mechanical properties but also for potential application implying a corrosive environment.

This study promoted the importance of targeting high cooling rate in thick plates of 6xxx aluminum alloys to avoid the presence of "soft areas", while it is leading to an heterogeneous response in terms of local mechanical behavior (Figure 5). The results are putting on perspective the usual $10°C.s^{-1}$ found in the literature while no clear boundary could be given as replacement if not targeting a specific property to improve.

5. Conclusion

The thermal treatments experienced in this study are on the edge of industrial capabilities. However, they are pointing out the difficulty of achieving an homogeneous quench when targeting high quenching rate on thick specimens and, either way, the difficulty to achieve an homogeneous quench with the fewer density of dispersoïds. Research on quenching impact has mostly been devoted to mechanical properties. With growing interest on 6xxx alloys for in-water application like off-shore wind turbines, research on microstructural changes and linked properties induced by quenching effect should be of primary interest. As $10°C.s^{-1}$ has been the most common quenching limit in the 6xxx aluminum industries overs years, results presented here a pushing onward the questionable nature of this boundary for 6xxx alloys designed for high end technologies.

6. Acknowledgments

This research was supported by the Material for Reactor Jules Horrowitz program (MT-RJH). The author want to address a peculiar acknowledgment to the Université Grenoble-Alpes SIMAP facility for its support.

References

[1] Jacobs et al., The structure of the metastable precipitates formed during ageing of an Al-Mg-Si alloy, Philosophical Magazine 26 (1978) 1–13.

[2] Ryum et al., Precipitation Reactions in an Aluminium 1wt.% Mg2si Allow, ZEITSCHRIFT FUR METALLKUNDE 70 (8) (1979) 528–535.

[3] Murayama et al., Pre-precipitates clusters and precipitation processes in Al-Mg-Si alloys, Acta Metallurgica 47 (5) (1999) 1537–1548.

[4] C.Barbosa, Identification of precipitates in 6013 aluminium alloy (Al-Mg-Si-Cu), ZEITSCHRIFT FUR METALLKUNDE 93 (3) (2002) 208–211.

[5] J. Banhart, C. S. T. Chang, Z. Liang, N. Wanderka, M. D. H. Lay, A. J. Hill, Natural Aging in Al-Mg-Si Alloys – A Process of Unexpected Complexity, Advanced Engineering Materials 12 (7) (2010) 559–571.
URL http://onlinelibrary.wiley.com/doi/10.1002/adem.201000041/abstract

[6] K. Matsuda, Y. Ishida, I. Mullerova, L. Frank, S. Ikeno, Cube-phase in excess Mg-type Al-Mg-Si alloy studied by EFTEM, Journal of Materials Science 41 (9) (2006) 2605–2610.
URL http://dx.doi.org/10.1007/s10853-006-7819-6

[7] L. Ding, Z. Jia, Z. Zhang, R. E. Sanders, Q. Liu, G. Yang, The natural aging and precipitation hardening behaviour of Al-Mg-Si-Cu alloys with different Mg/Si ratios and Cu additions, Materials Science and Engineering: A 627 (2015) 119–126.
URL http://www.sciencedirect.com/science/article/pii/S092150931401586X

[8] A. Jaafar, A. Rahmat, Z. Hussain, I. Zainol, Effect of Mg, Si and Cu content on the microstructure of dilute 6000 series aluminium alloys, Journal of Alloys and Compounds 509 (35) (2011) 8632 – 8640.
URL http://www.sciencedirect.com/science/article/pii/S0925838811011571

[9] A. Abúndez, I. Pereyra, B. Campillo, S. Serna, E. Alcudia, A. Molina, A. Blanco, J. Mayén, Improvement of ultimate tensile strength by artificial ageing and retrogression treatment of aluminium alloy 6061, Materials Science and Engineering: A 668 (2016) 201 – 207.
URL http://www.sciencedirect.com/science/article/pii/S0921509316305688

[10] M. Farshidi, M. Kazeminezhad, H. Miyamoto, On the natural aging behavior of Aluminum 6061 alloy after severe plastic deformation, Materials Science and Engineering: A 580 (2013) 202–208.
URL http://www.sciencedirect.com/science/article/pii/S0921509313005911

[11] W. Ma, B. Wang, L. Yang, X. Tang, W. Xiao, J. Zhou, Influence of solution heat treatment on mechanical response and fracture behaviour of aluminium alloy sheets: An experimental study, Materials & Design 88 (2015) 1119–1126.
URL http://www.sciencedirect.com/science/article/pii/S0264127515304548

[12] R. R. Ambriz, D. Chicot, N. Benseddiq, G. Mesmacque, S. D. d. l. Torre, Local mechanical properties of the 6061-T6 aluminium weld using micro-traction and instrumented indentation, European Journal of Mechanics - A/Solids 30 (3) (2011) 307 – 315.
URL http://www.sciencedirect.com/science/article/pii/S0997753810001452

[13] D. Maisonnette, M. Suery, D. Nelias, P. Chaudet, T. Epicier, Effects of heat treatments on the microstructure and mechanical properties of a 6061 aluminium alloy, Materials Science and Engineering: A 528 (6) (2011) 2718 – 2724.
URL http://www.sciencedirect.com/science/article/pii/S0921509310014048

[14] G. Mrówka-Nowotnik, J. Sieniawski, Influence of heat treatment on the microstructure and mechanical properties of 6005 and 6082 aluminium alloys, Journal of Materials Processing Technology 162–163 (2005) 367–372.
URL http://www.sciencedirect.com/science/article/pii/S0924013605002207

[15] J. L. Cavazos, R. Colás, Precipitation in a heat-treatable aluminum alloy cooled at different rates, Materials Characterization 47 (3–4) (2001) 175 – 179.
URL http://www.sciencedirect.com/science/article/pii/S1044580301001644

[16] J. L. Cavazos, R. Colás, Quench sensitivity of a heat treatable aluminum alloy, Materials Science and Engineering: A 363 (1–2) (2003) 171 – 178.
URL http://www.sciencedirect.com/science/article/pii/S0921509303006166

[17] K. Strobel, M. A. Easton, L. Sweet, M. J. Couper, J.-F. Nie, Relating Quench Sensitivity to Microstructure in 6000 Series Aluminium Alloys, Materials Transactions, JIM 52 (5) (2011) 914–919.
URL http://ci.nii.ac.jp/naid/130004454718/en/

[18] J. Davis, A. I. H. Committee, Metals Handbook Desk Edition 2nd Edition, 75th anniversary ASM handbooks, Taylor & Francis, 1998.
URL https://books.google.co.in/books?id=IpEnvBtSfPQC

[19] G. E. Totten, D. S. MacKenzie, Handbook of Aluminum: Vol. 1: Physical Metallurgy and Processes, CRC Press, 2003.

[20] P. Schumacher, S. Pogatscher, M. J. Starink, C. Schick, V. Mohles, B. Milkereit, Quench-induced precipitates in Al–Si alloys: Calorimetric determination of solute content and characterisation of microstructure, Thermochimica Acta 602 (2015) 63–73.
URL http://www.sciencedirect.com/science/article/pii/S0040603115000192

[21] I. Dutta, S. M. Allen, A calorimetric study of precipitation in commercial aluminium alloy 6061, Journal of Materials Science Letters 10 (6) (1990) 323–326.
URL http://dx.doi.org/10.1007/BF00719697

[22] K. Buchanan, J. Ribis, J. Garnier, K. Colas, Identification of monoclinic θ-phase dispersoids in a 6061 aluminium alloy, Philosophical Magazine Letters 0 (0) (2016) 1–11.
URL http://www.tandfonline.com/doi/abs/10.1080/09500839.2016.1162911

[23] S. Claves, D. Elias, W. Z. Misiolek, Analysis of the Intermetallic Phase Transformation Occurring during Homogenization of 6xxx Aluminum Alloys, Trans Tech Publications, Zuerich-Uetikon, Switzerland, 2002.

[24] N. Wang, Z. Zhou, G. Lu, Microstructural Evolution of 6061 Alloy during Isothermal Heat Treatment, Journal of Materials Science & Technology 27 (1) (2011) 8 – 14.
URL http://www.sciencedirect.com/science/article/pii/S1005030211600182

[25] T. Saito, C. D. Marioara, J. Røyset, K. Marthinsen, R. Holmestad, The effects of quench rate and pre-deformation on precipitation hardening in Al–Mg–Si alloys with different Cu amounts, Materials Science and Engineering: A 609 (2014) 72–79.
URL http://www.sciencedirect.com/science/article/pii/S0921509314005589

[26] CEA, DEN, DM2s, SEMT, Cast3m.
URL http://www-cast3m.cea.fr/

[27] E. Rauch, J. Portillo, S. Nicolopoulos, D. Bultreys, S. Rouvimov, P. Moeck, Automated nanocrystal orientation and phase mapping in the transmission electron microscope on the basis of precession electron diffraction, Zeitschrift fur Kristallographie 225 (2-3) (2010) 103–109.

[28] E. Rauch, M. Veron, J. Portillo, D. Bultreys, Y. Maniette, S. Nicolopoulos, Automatic crystal orientation and phase mapping in TEM by precession diffraction, Microsc. Anal. 22 (93) (2008) S5–S8.

[29] S. M. Cho, Analytical methods in conduction heat transfer, Glen E. Myers, McGraw-Hill Book Company, New York (1971). 508 pages. $19.50, AIChE Journal 18 (4) (1972) 879–879.
URL https://onlinelibrary.wiley.com/doi/abs/10.1002/aic.690180448

[30] L. Lodgaard, N. Ryum, Precipitation of dispersoids containing Mn and/or Cr in Al–Mg–Si alloys, Materials Science and Engineering: A 283 (1–2) (2000) 144 – 152.
URL http://www.sciencedirect.com/science/article/pii/S0921509300007346